Correlated nonreciprocity around conjugate exceptional points

Arnab Laha,[1,2,*] Adam Miranowicz,[1] R. K. Varshney,[2] and Somnath Ghosh[3]
[1]*Institute of Spintronics and Quantum Information, Faculty of Physics, Adam Mickiewicz University, 61-614 Poznań, Poland*
[2]*Department of Physics, Indian Institute of Technology Delhi, New Delhi 110016, India*
[3]*Department of Physics, Indian Institute of Technology Jodhpur, Rajasthan 342037, India*

(Received 26 August 2023; accepted 23 February 2024; published 8 March 2024)

The occurrence of exceptional points (EPs) is a fascinating non-Hermitian feature of open systems. A level-repulsion phenomenon between two complex states of an open system can be realized by positioning an EP and its time-reversal ($\mathcal{T}$) conjugate pair in the underlying parameter space. Here, we report interesting nonreciprocal responses of such two conjugate EPs by using a dual-mode planar waveguide system having two $\mathcal{T}$-symmetric active variants concerning the transverse gain-loss profiles. We specifically reveal an all-optical scheme to achieve correlative nonreciprocal light dynamics by using the reverse chirality of two dynamically encircled conjugate EPs in the presence of local nonlinearity. A specific nonreciprocal correlation between two designed $\mathcal{T}$-symmetric waveguide variants is established in terms of their unidirectional transfer of light with a precise selection of modes. Here, the unconventional reverse chiral properties of two conjugate EPs allow the nonreciprocal transmission of two selective modes in the opposite directions of the underlying waveguide variants. An explicit dependence of the nonlinearity level on a significant enhancement of the nonreciprocity in terms of an isolation ratio is explored by investigating the effects of both local Kerr-type and saturable nonlinearities (considered separately). The physical insights and implications of harnessing the features of conjugate EPs in nonlinear optical systems can enable the growth and development of a versatile platform for building nonreciprocal components and devices.

DOI: 10.1103/PhysRevA.109.033511

I. INTRODUCTION

The synergy of non-Hermitian quantum physics and photonics has been revealing a novel and promising direction for building a range of photonics components and devices [1]. An extensive study on the perturbation theory in quantum mechanics once revealed the occurrence of exceptional point (EP) singularities as an explicit mathematical feature of non-Hermitian or open systems [2]. EPs usually appear as topological defects in the system's parameter space, affecting the eigenspace dimensionality, which results in the simultaneous coalescence of at least two coupled eigenvalues and the associated eigenstates [2–6]. The parity-time ($\mathcal{PT}$)-symmetric systems (a special class of non-Hermitian system with real eigenvalues) [7,8] encounter an EP at a spontaneous transition from real (exact-$\mathcal{PT}$-phase) to complex (broken-$\mathcal{PT}$-phase) eigenvalues [9–12]. Recently, the engineering of ubiquitous non-Hermitian components (e.g., loss and gain) in photonic systems has revealed such EP-like mathematical objects as a powerful tool to manipulate and detect the energy-states of light [11–17]. A controlled parametric variation in the vicinity of EPs can immensely boost a versatile range of quantum-photonic technologies in the context of, e.g., asymmetric energy transfer [18], programmable state-switching [19,20], phonon lasing [21], coherent perfect absorption [22], slow-light engineering [23], enhanced energy harvesting [24], parametric instability [25], and highly precise sensing [26,27].

The concept of the occurrence of conjugate EPs has recently been introduced based on the complex parameter dependence of a non-Hermitian Hamiltonian [28]. This can be described by considering a generic two-level (without loss of generality for higher-order situations) non-Hermitian Hamiltonian $\mathcal{H}(\lambda)$, which depends on a complex parameter $\lambda = \lambda^{\mathrm{R}} + i\lambda^{\mathrm{I}}$. The associated eigenvalues $\mathcal{E}_{1,2}(\lambda)$ and the eigenvectors $\Psi_{1,2}(\lambda)$ would be analytical functions in the complex-λ plane except at a singularity $\lambda = \lambda_s$, known as an EP. Concerning the imaginary part of the dependent parameter λ (i.e., λ^{I}), the considerations of $\lambda^{\mathrm{I}} < 0$ and $\lambda^{\mathrm{I}} > 0$ ideally define two complementary variants of $\mathcal{H}(\lambda)$. Such two complementary systems can be correlated based on time-reversal ($\mathcal{T}$) symmetry. Here, two variants of $\mathcal{H}(\lambda)$ under $\mathcal{T}$-symmetry separately host two EPs in the complex λ plane at $\lambda_s = \lambda_s^{\mathrm{R}} + i\lambda_s^{\mathrm{I}}$ and $\lambda_s^* = \lambda_s^{\mathrm{R}} - i\lambda_s^{\mathrm{I}}$ (say, EP and its conjugate EP*, respectively), which are in the complex conjugate relation. Such two correlated EPs in two $\mathcal{T}$-symmetric complementary systems can be called as conjugate EPs.

Unconventional light guidance mechanism based on the chirality of EPs has extensively been studied, where a sufficiently slow length-dependent gain-loss dynamics along a closed two-dimensional (2D) loop around an EP can steer the adiabatic and nonadiabatic conversions of modes [29,30]. Here, even though the adiabaticity is maintained in the sense of the exchange of eigenvalues for a quasistatic gain-loss variation [31], the associated eigenmodes fail to meet adiabaticity while propagating along the length, which results in the conversion of all the modes into different particular dominating modes, based on the device chirality (in terms of

*arnablaha777@gmail.com

direction of light propagation) [32–36]. Such a chirality-based asymmetric transfer of modes has recently been explored to reveal a distinct reverse-chiral behavior of a pair of conjugate EPs, while dynamically encircling them in two $\mathcal{T}$-symmetric active variants of a waveguide-based optical system [28].

Moreover, the reciprocity of such a chiral light dynamics can be broken by introducing nonreciprocal elements, where the occurrence of an EP can considerably enhance nonreciprocity [37,38]. Nonreciprocal devices, such as isolators and circulators, allow only one-way light transmission with an asymmetric scattering matrix, which is indispensable to minimize unwanted back-reflection and multi-path interference in photonic circuits [39]. However, the common magnetooptical approaches (such as a Faraday rotator), mainly applied for bulky free-space devices, are usually inefficient in enabling a sufficient nonreciprocity for photonic circuits. Hence, there are growing demands to achieve high nonreciprocity on the chip-scale footprint, where the chiral response of an EP in nonlinear media can play a crucial role in meeting such demands. Recently, an EP-induced mode-selective isolation scheme has been revealed, where local nonlinearity has served as an efficient tool to enable all-optical nonreciprocity without using any magneto-optical effect [36]. In this context, the chiral response of two conjugate EPs in nonlinear media could have immense potential in developing correlative nonreciprocal devices with highly precise mode manipulation. Moreover, the recently developed non-Hermitian formalism of Liouvillian superoperators [40,41] can also be exploited for the quantum implementation of our waveguide-based classical analysis to explore the correlated features of conjugate quantum EPs.

In this article, we comprehensively report the correlated nonreciprocal response of two $\mathcal{T}$-symmetric active variants of a gain-loss assisted dual-mode planar waveguide, operating near two conjugate EPs. Here, all-optical nonreciprocity is achieved with the introduction of local nonlinearity. We investigate the hosting of conjugate EPs in complementary gain-loss parameter planes based on Riemann surface connections associated with two quasi-guided modes. Besides establishing the reverse-chiral response concerning the asymmetric mode conversion process driven by dynamical parametric variation in the vicinity of two conjugate EPs, we exclusively investigate the asymmetric nonreciprocal waveguidence mechanism in the context of all-photonic isolation through two $\mathcal{T}$-symmetric waveguide variants. Here, a correlation in the nonreciprocal transmission of selective modes with an enhanced isolation ratio (say, IR) through two complementary waveguides is established. Moreover, a comparative study on the individual effect of local Kerr-type nonlinearity and saturable nonlinearity is reported by showing the possibility of enhancing the IR significantly.

II. RESULTS AND DISCUSSION

A. Designing two time-symmetric active waveguide variants

To explore the correlated nonreciprocity in two $\mathcal{T}$-symmetric waveguide variants, we design a framework consisting of a 2D planar step-index optical waveguide. The geometrical dimensions of the designed waveguide are considered as $w = 20\lambda/\pi$ (width) and $l = l_m \times 10^3$ (length) with $l_m = 7.5\lambda/\pi$ (i.e., both the dimensions are considered in the unit of wavelength λ). We set $\lambda = 2\pi$ corresponding to a normalized wave number $k = 1$ to consider the entire operation in dimensionless units. The waveguide, consisting of a core and a surrounded cladding (with the refractive indices $n_{\rm co}$ and $n_{\rm clad}$, respectively), is distributed in the xz plane, where $x \in [-w/2, w/2]$ and $z \in [0, l]$ are the transverse and propagation axes, respectively. The real (background) refractive index profile is considered as

$$\mathrm{Re}[n(x)] = \begin{cases} n_{\rm co} & : -w/6 \leqslant x \leqslant w/6, \\ n_{\rm clad} & : w/6 \leqslant |x| \leqslant w/2. \end{cases} \tag{1}$$

We determine $n_{\rm co} = 1.5$ and $n_{\rm clad} = 1.46$, for which the designed waveguide can be realized with glass- and silica-based material combinations in a fabrication-feasible platform. Based on the chosen dimensional parameters and Re$[n(x)]$ profile, the designed waveguide supports only two scalar modes: the fundamental mode $\Psi_{\rm F}$ and the first higher-order mode $\Psi_{\rm H}$.

Now, we enable non-Hermiticity via the introduction of an unbalanced gain-loss profile [i.e., the imaginary part of $n(x)$] in the designed passive waveguide, which results in the coupling between two quasiguided modes $\Psi_{\rm F}$ and $\Psi_{\rm H}$. We can control such coupling with the modulation of a gain-loss profile in a 2D parameter space characterized by the gain-loss coefficient γ and a loss-to-gain ratio τ. Using this waveguide framework, we consider two complementary active variants

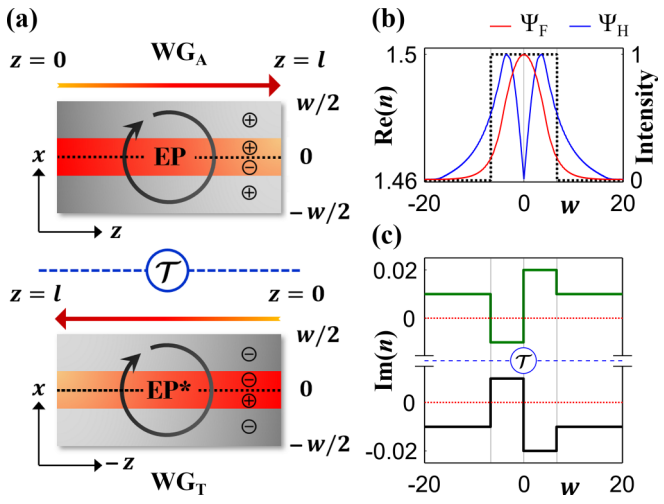

FIG. 1. (a) Schematic design of $\mathrm{WG_A}$ and $\mathrm{WG_T}$ ($\mathcal{T}$ symmetric) based on the framework of a gain-loss assisted planar waveguide. Two arrows indicate their opposite propagation directions. Circular plus and minus signs in different segments are associated with the positive (loss) and negative (gain) imaginary indices as in Eq. (2). (b) Transverse background refractive index profile, i.e., Re$[n(x)]$, (dotted black line; corresponding to the left vertical axis) along with normalized intensity profiles of two supported modes $\Psi_{\rm F}$ and $\Psi_{\rm H}$ (corresponding to the right vertical axis). (c) Transverse gain-loss distributions, i.e., Im$[n(x)]$, for two $\mathcal{T}$-symmetric variants $\mathrm{WG_A}$ (solid green line) and $\mathrm{WG_T}$ (solid black line) for $\gamma = 0.01$ and $\tau = 2$. w and l ($= l_m \times 10^3$) are considered in units of λ.

connected via $\mathcal{T}$-symmetric Im$[n(x)]$ profiles given by

$$\mathrm{Im}[n(x)] = \begin{cases} -i\gamma & | & +i\gamma & : -w/6 \leqslant x \leqslant 0, \\ +i\tau\gamma & (\mathcal{T}) & -i\tau\gamma & : 0 \leqslant x \leqslant w/6, \\ +i\gamma & | & -i\gamma & : w/6 \leqslant |x| \leqslant w/2. \end{cases} \quad (2)$$

Such two $\mathcal{T}$-symmetric waveguide variants, say $\mathrm{WG_A}$ and $\mathrm{WG_T}$ are shown in Fig. 1(a). Figure 1(b) shows the profile of Re$[n(x)]$ [dotted black line; given by Eq. (1)] of the background framework along with the normalized intensity profile of two symmetric scalar modes Ψ_F and Ψ_H supported by the passive waveguide (i.e., when $\gamma = 0$). Here, the validation of scalar modal analysis based on Maxwell's equations is justified for computing the mode profiles, as we considered a small index difference between the core and cladding ($\Delta n = 0.04$). Figure 1(c) shows the profiles of Im$[n(x)]$ of two active variants $\mathrm{WG_A}$ and $\mathrm{WG_T}$ (represented by green and black lines, respectively) for a specifically chosen $\gamma = 0.01$ and $\tau = 2$.

As per the constraints of $\mathcal{T}$ symmetry, i.e., $\mathcal{T} : \{i, t, x\} \rightarrow \{-i, -t, x\}$ (i is the imaginary quantity; t and x are the time and space coordinates, respectively), $\mathrm{WG_A}$ and $\mathrm{WG_T}$ host exactly two complex conjugate profiles of $n(x)$ with respect to the transverse axis [as can be understood from Eq. (2) and Fig. 1(c)]. Here, we have to consider two opposite propagation directions for $\mathrm{WG_A}$ and $\mathrm{WG_T}$ to maintain $\mathcal{T}$-symmetric equivalence based on the quantum-optical analogy $t \equiv z$. Now, we initially host two conjugate EPs in the gain-loss parameter space of two $\mathcal{T}$-symmetric waveguide variants while operating in the linear regime. After establishing the reverse chiral response of two conjugate EPs in the linear regime, we introduce nonlinearity to explore the nonreciprocal effects and the corresponding correlations.

In this context, the independent variations of γ and τ [i.e., Im(n)], irrespective of the chosen Re(n)-profile, must adhere to the Kramers-Kronig causality condition. This requirement is particularly crucial in our context, as we consider a patterned gain-loss profile (which is also applicable to $\mathcal{PT}$-symmetric systems) to encounter conjugate EPs. Fulfilling the causality condition is feasible only for a discrete frequency and cannot be achieved across any finite frequency range [42]. Consequently, we focus on performing the overall study for a single operating frequency ($k = 1$) to fulfill the causality relation [43]. As a result, the dispersive effects of core and cladding materials can safely be disregarded.

B. Riemann surface connections: Hosting conjugate EPs

To host the pair of conjugate EPs, we study the interaction between two coupled eigenvalues associated with Ψ_F and Ψ_H, while varying the control parameters γ and τ, simultaneously, within chosen ranges. Toward elucidating the phenomenon of the hosting of conjugate EPs, a comprehensive analytical treatment based on a non-Hermitian Hamiltonian, which is analogous to our proposed waveguide-based system, is undertaken. The detailed discussion can be found in the Appendix.

For our waveguide system, the complex propagation constants (β values), i.e., β_F and β_H (associated with Ψ_F and Ψ_H, respectively) are considered as the eigenvalues, which are calculated by computing the solutions of the 1D scalar wave equation $[\partial_x^2 + k^2 n^2(x) - \beta^2]\psi(x) = 0$. We identify the connections between the Riemann sheets associated with coupled β_F and β_H in Fig. 2(a) [with the distributions of Re(β) and Im(β) as shown in Figs. 2(a.1) and 2(a.2)], where the formation of a pair of conjugate EPs is clearly evident. The dotted red and blue curves show the trajectories of β_F and β_H concerning a continuous variation of γ, when we particularly choose $\tau = 3.1607$. Here, we can observe a simultaneous bifurcation and a coalescence of the associated Re(β) and Im(β) values at $\gamma = -8.1 \times 10^{-3}$, as in Figs. 2(a.1) and 2(a.2), respectively. In contrary, a simultaneous coalescence and bifurcation of the associated Re(β) and Im(β) values can be observed at $\gamma = 8.1 \times 10^{-3}$. Hence, two different circumstances corresponding to $\gamma < 0$ and $\gamma > 0$ for a specific τ refers to perfect complex conjugate situations (as the parameters γ and τ are associated with Im$[n(x)]$, i.e., gain-loss), which can ideally be observed in two active variants $\mathrm{WG_A}$ and $\mathrm{WG_T}$. The associated characteristics of β_F and β_H refer to the encounter of two conjugate EPs at $(\pm 8.1 \times 10^{-3}, 3.1607)$ (say, an EP and its conjugate EP* for $\mathrm{WG_A}$ and $\mathrm{WG_T}$, respectively) in the respective (γ, τ) planes. Topological dissimilarities in ARC-type interactions between β_F and β_H can clearly be observed alongside these conjugate EPs. The coalescence of the eigenmodes (Ψ_F and Ψ_H) at both the conjugate EPs can be understood from the variation of $\langle \Psi_\mathrm{F} | \Psi_\mathrm{H} \rangle$ with γ at a fixed $\tau = 3.1607$, where $\langle \Psi_\mathrm{F} | \Psi_\mathrm{H} \rangle = 1$ only at EP and EP*, as shown in Fig. 2(b).

The effect of parametric encirclement of the embedded conjugate EPs in terms of chiral branch-point features is investigated in Fig. 2(c). Here, we consider two parametric loops in the 2D (γ, τ) plane according to the equations

$$\gamma(\varphi) = \gamma_c \sin\left(\frac{\varphi}{2}\right) \quad \text{and} \quad \tau(\varphi) = \tau_c + r\sin(\varphi), \quad (3)$$

which leads to a closed and simultaneous variation of gain and loss around the EP and EP*. A slow variation of $\varphi \in [0, 2\pi]$ governs the stroboscopic encirclements based on the characteristic parameters γ_c, τ_c, and $r \in (0, 1]$, where the conjugate EPs would be inside the parametric loop only for $|\gamma_c| > |\gamma_\mathrm{EP}|$ ($\gamma_\mathrm{EP} = 8.1 \times 10^{-3}$; γ value at the location of the EP). Here, the variations $\varphi : 0 \rightarrow 2\pi$ and $\varphi : 0 \leftarrow 2\pi$ enable a clockwise (CW) and a counterclockwise (CCW) gain-loss variation around the EP for $\gamma_c > 0$, and vice versa around the EP* for $\gamma_c < 0$. Such two parametric loops are shown in the ground surfaces of both Figs. 2(c.1) and 2(c.2) (for $r = 0.3$, $\gamma_c = \pm 1.5 \times 10^{-2}$. and $\tau_c = 3.1607$), where the associated trajectories of coupled β_F and β_H are shown on their respective Riemann surfaces. Here, we observe that β_F and β_H are swapping their identities from their respective surfaces [concerning both Re(β) and Im(β), as can be seen in Figs. 2(c.1) and 2(c.2), respectively], and exchange their initial positions upon the completion of encirclement schemes. Such switching between complex β_F and β_H around both EP and EP* justify their branch-point behavior.

C. Dynamically encircled conjugate EPs: Asymmetric transfer of modes in a linear medium

Here, we investigate the correlative dynamics of the light (modes) propagation in the linear regime while encircling the conjugate EPs dynamically. The correlation is elucidated from a chiral perspective, highlighting the reciprocal

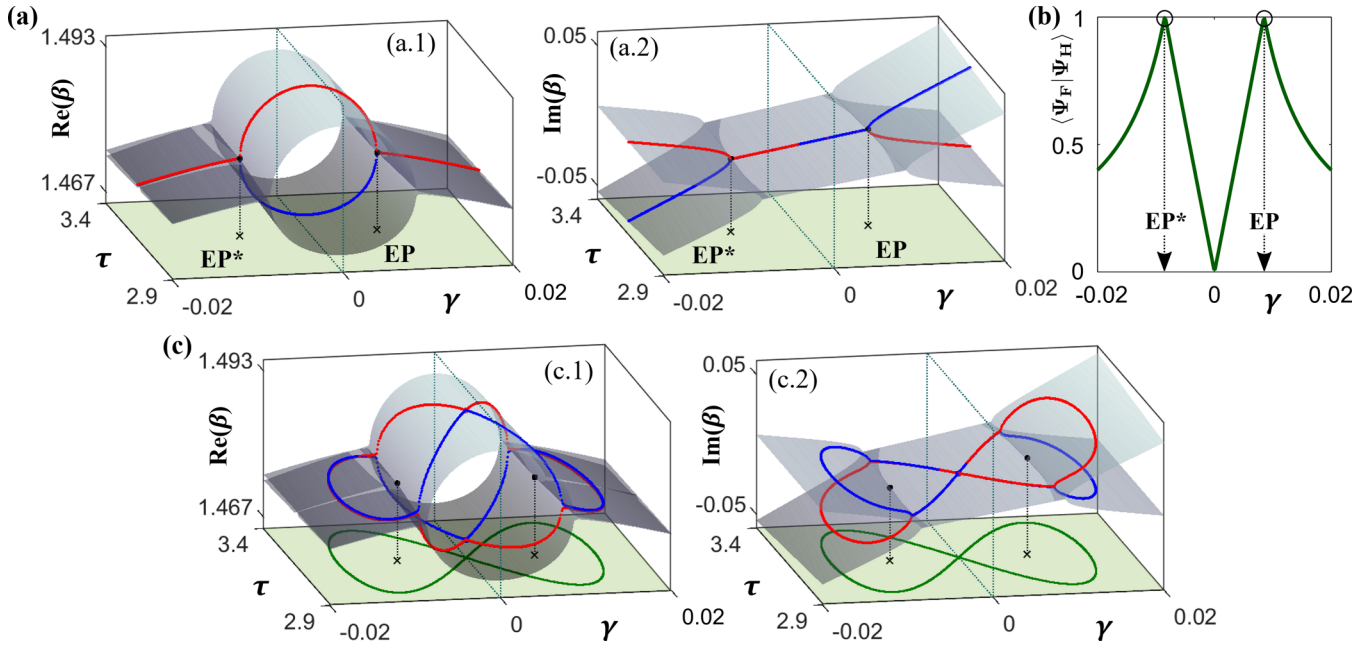

FIG. 2. (a) Connections between the Riemann surfaces associated with β_F and β_H, while varying the control parameters γ and τ, simultaneously. (a.1) and (a.2) show the distributions of Re[β] and Im[β], respectively. Dotted red and blue curves represent the trajectories of β_F and β_H for a chosen $\tau = 3.1607$, which reveal the encounter of two conjugate EPs based on the coalescence and bifurcations in Re[β] and Im[β] at $\gamma = \pm 8.1 \times 10^{-3}$. Dotted blue squares separate the regions for WG_A and WG_T. (b) Variation of $\langle\Psi_F|\Psi_H\rangle$ with respect to γ (when $\tau = 3.1607$), which shows the coalescence of Ψ_F and Ψ_H via $\langle\Psi_F|\Psi_H\rangle = 1$ at both EP and EP*. (c) Parametric encirclement of two conjugate EPs in the (γ, τ)-plane following Eq. (3) (shown in the ground surfaces) and associated transfer process of β_F and β_H from their respective surfaces.

direction-dependent response of the device. Such an understanding would establish a promising foundation, paving the way for nonreciprocal behaviors upon the introduction of nonlinearity. We consider the length dependence (analogous to the time dependence) on the gain-loss parameter space to host dynamical encirclement schemes in two $\mathcal{T}$-symmetric waveguide variants. Figure 3(a) shows the chosen parametric loops for WG_A and WG_T [to encircle EP and EP*; exactly the same loops, as can be seen in the ground surfaces of Fig. 2(c)]. We map the associated gain-loss distribution along the length (z axis) of respective waveguides. Here, the reversal of the time axis ($t \to -t$) under the constraint of $\mathcal{T}$ symmetry allows us to consider mapping obligatorily in opposite directions (i.e., $z \to -z$ as $t \equiv z$) for WG_A and WG_T. Hence, we distribute the gain-loss profile from $z = 0$ to $z = l$ based on the encirclement of EP (EP*) governed by $\varphi : 0 \to 2\pi$ ($\varphi : 2\pi \to 0$) for WG_A (WG_T). Such a z-dependent gain-loss distribution can be implemented by reconsidering Eq. (3) as a function of z as

$$\gamma(z) = \gamma_c \sin\left(\frac{\pi z}{l}\right) \quad \text{and} \quad \tau(z) = \tau_c + r \sin\left(\frac{2\pi z}{l}\right). \tag{4}$$

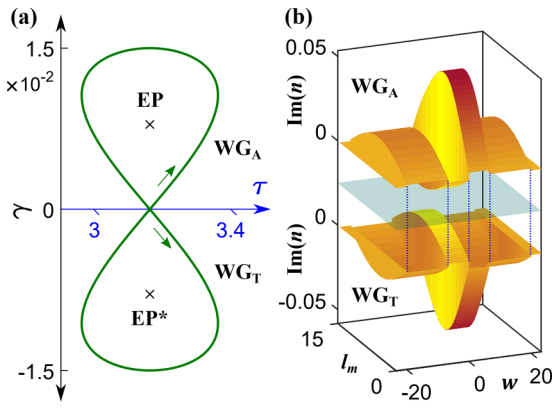

FIG. 3. (a) Parametric loops to encircle an EP and its conjugate EP* in the (γ, τ) plane [following Eq. (3)]. (b) Associated dynamical variation of gain-loss profiles, i.e., two complex conjugate active potentials (separated via a transparent plane), experienced by two $\mathcal{T}$-symmetric waveguide variants WG_A and WG_T. w and l ($= l_m \times 10^3$) are considered in units of λ.

Figure 3(b) shows two complex conjugate 2D Im(n) profiles [governed by Eq. (4)] to encircle the EP and EP* dynamically. Such a parameter space allows the recovery of symmetric modes (passive) while considering propagation in any of two directions (as $\gamma = 0$ at both $z = 0$ and $z = l$). Here, the CW and CCW directions of encirclements are realized through one complete pass of light in the forward direction ($z : 0 \to l$) and backward direction ($z : l \to 0$), respectively, for WG_A, and vice versa for WG_T.

Now, we implement the scalar beam propagation method to investigate the individual light transmission through WG_A and WG_T. The characteristic beam propagation equation of an input beam can be written as

$$-2ik\partial_z\Psi(x,z) = \left[\partial_x^2 + k^2\Delta n^2(x,z)\right]\Psi(x,z), \tag{5}$$

with $\Delta n^2(x,z) \equiv n^2(x,z) - n_{\text{clad}}^2$, which is generally formulated as a solution to the Helmholtz equation under paraxial and slowly varying-envelope approximations. We develop a MATLAB code to implement the beam propagation method based on Eq. (5) by using a split-step analysis. Here, we consider the active Δn profile (non-Hermitian) and compute Eq. (5) for both Ψ_F and Ψ_H with extremely fine split-step computation. Similar beam propagation investigations can be performed in feasible three-dimensional (3D) systems based on coupled waveguide and fiber geometries, where an extended approach of our proposed theoretical model can be implemented with appropriate numerical methods [44]. Recently, a gain-loss assisted dual-core fiber system implementing a dynamical encirclement of a second-order EP was reported as a potential 3D platform [45].

Figure 4 shows the resultant propagation characteristics, while considering the dynamical encirclements around the EP and EP* in WG_A and WG_T, respectively. Here, we initially verify the linear response (i.e., without any nonlinearity) in the context of an asymmetric transfer between the

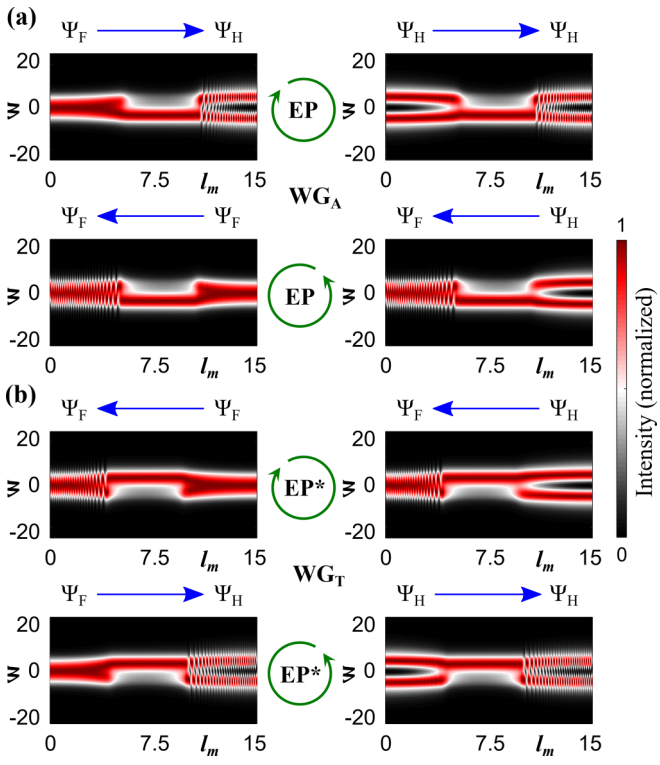

FIG. 4. (a) Propagation dynamics of Ψ_F and Ψ_H through WG_A (upper panel) from $z = 0$ to $z = l$ (associated with the CW dynamical EP encirclement) followed by the asymmetric conversions $\{\Psi_F, \Psi_H\} \to \Psi_H$; (lower panel) from $z = l$ to $z = 0$ (associated with the CCW dynamical EP encirclement) followed by the asymmetric conversions $\{\Psi_F, \Psi_H\} \to \Psi_F$. (b) Similar modal dynamics through WG_T (upper panel) for the CW dynamical encirclement around the EP* with $z : l \to 0$, exhibiting the asymmetric conversions $\{\Psi_F, \Psi_H\} \to \Psi_F$; (lower panel) for the CCW dynamical encirclement around the EP* with $z : 0 \to l$, exhibiting the asymmetric conversions $\{\Psi_F, \Psi_H\} \to \Psi_H$. Intensities are renormalized at each step of evolution along z to show the inputs and outputs clearly. w and l $(= l_m \times 10^3)$ are considered in units of λ.

modes, which occurs due to the failure of the adiabatic approximation led by a dynamically encircled EP, despite the associated omnipresent β-switching process. Here, the EP (or EP*) itself acts as a source of chirality, which mainly steers the response of the underlying system in the context of a direction-dependent transfer of modes. Such an unconventional modal dynamics can be observed for both WG_A and WG_T, as shown in Figs. 4(a) and 4(b), respectively.

To enable a dynamical encirclement of the EP in the CW direction, we consider the propagation of light from $z = 0$ to $z = l$ (forward direction) in WG_A. We can observe the corresponding dynamics of Ψ_F and Ψ_H in the upper panel of Fig. 4(a), where Ψ_F is converted into Ψ_H, following the adiabatic expectation. However, Ψ_H violets the system adiabaticity, i.e., it becomes restructured and remains as Ψ_H. Thus a light signal launched at $z = 0$ of WG_A is converted into a dominating Ψ_H at $z = l$. The lower panel of Fig. 4(a) shows the modal transitions, while considering light propagation in the backward direction ($z : l \to 0$; associated with the CCW encirclement process). Here, Ψ_F dominates at the output $z = 0$ with the asymmetric conversions $\{\Psi_F, \Psi_H\} \to \Psi_F$, where only Ψ_H maintains the adiabatic expectations (unlike the case for the CW encirclement process). Thus during the dynamical encirclement of an EP, the system partially maintains the adiabaticity, which however turns into a fascinating chiral light dynamics, where irrespective of the excited modes at the input, the device delivers two different dominating modes in the opposite directions.

Such a violation in the system adiabaticity around an EP, can be predicted with the associated nonadiabatic correction terms ($\mathbb{N}_{F\to H}$ and $\mathbb{N}_{H\to F}$ for the adiabatic expectations $\Psi_F \to \Psi_H$ and $\Psi_H \to \Psi_F$, respectively) from the adiabatic theorem [29]. These corrections mainly rely on the accumulated relative-gain ($\Delta\gamma_{F,H}^{ad}$) factor during the transition of modes as (generalized with a quantum-optical analogy under the operating condition)

$$\mathbb{N}_{F\{H\}\to H\{F\}} \propto -\{+\} \exp \int_0^l \Delta\gamma_{F,H}^{ad}(\gamma, \tau) dz. \tag{6}$$

Here, $\Delta\gamma_{F,H}^{ad}$ can be estimated from the relative difference between the average loss (γ^m) accrued by the individual modes. The adiabatic trajectories of $\text{Im}(\beta)$ values [as shown in Fig. 2(c.2)] for Ψ_F and Ψ_H gives the associated γ^m with $\oint\{\text{Im}(\beta)/2\pi\}d\varphi$.

Here, the variant WG_A operating with a dynamically encircled EP gives $\Delta\gamma_{F,H}^{ad} > 0$ for the CW direction, whereas $\Delta\gamma_{F,H}^{ad} < 0$ for the CCW direction. These particular relations result in the domination of the $\mathbb{N}$ factor associated with the amplifying exponent of $\Delta\gamma_{F,H}^{ad}$ over the overall adiabatic expectations, whereas cooperation of the $\mathbb{N}$ factor corresponding to the decaying exponent of $\Delta\gamma_{F,H}^{ad}$ with the adiabatic expectations. Hence, the domination of $\mathbb{N}_{H\to F}$ in the forward direction yields the nonadiabatic transition of $\Psi_H(\to \Psi_H)$, whereas the cooperation of $\mathbb{N}_{F\to H}$ supports the adiabatic conversion of $\Psi_F(\to \Psi_H)$. On the other hand, the domination of $\mathbb{N}_{F\to H}$ in the backward direction yields the nonadiabatic transition of $\Psi_F(\to \Psi_F)$, whereas the cooperation of $\mathbb{N}_{H\to F}$ supports the adiabatic conversion of $\Psi_H(\to \Psi_F)$. The detailed analytical predictions completely support our numerical

beam-propagation results for WG_A, as shown in Fig. 4(a). From the dependence of the relative-gain factor $\Delta\gamma^{ad}_{F,H}$ on the EP-induced asymmetric mode conversions, one can generically conclude that the mode transiting with a lower average loss (γ^m) follows the adiabatic rules, whereas its coupled counterpart evolves nonadiabatically.

Now, if we consider the dynamical encirclement around EP*, then the concerned waveguide variant WG_T exhibits reverse-chiral dynamics compared to the chiral behavior of WG_A, as can be seen in Fig. 4(b). During the encirclement in the CW directions, Ψ_F and Ψ_H transmit along the backward direction ($z : l \to 0$) with $\Delta\gamma^{ad}_{F,H} < 0$, which allows the nonadiabatic transfer of Ψ_F and the adiabatic transfer of Ψ_H with the asymmetric conversions $\{\Psi_F, \Psi_H\} \to \Psi_F$ at $z = 0$ [as shown in the upper panel of Fig. 4(b)]. In this case, Ψ_H evolves with a lower γ^m and maintains the adiabatic expectations. In contrary, the modal transmissions in the forward direction ($z : 0 \to l$) of WG_T with a positive relative-gain factor ($\Delta\gamma^{ad}_{F,H} > 0$) yields the delivery of the dominating Ψ_F with the asymmetric conversions $\{\Psi_F, \Psi_H\} \to \Psi_H$, while considering the encirclement in the CCW direction [as shown in the lower panel of Fig. 4(b)]. Here, Ψ_F evolves with a lower γ^m and maintains the adiabatic expectations. Hence, based on the constraints of the $\mathcal{T}$ symmetry, we exclusively demonstrate interesting opposite chiral responses of two active variants designed on the same background waveguide system, where the opposite encirclement directions around the EP and EP* result in the delivery of modes of the same order.

D. Effect of nonlinearity on the asymmetric state-transfer process: Enabling nonreciprocity around two conjugate EPs

The direction-dependent light transmission process with the asymmetric transfer of modes (as described for two waveguide variants) can be understood by a scattering matrix (S-matrix) relation. We meticulously formulate an S matrix to encompass all possible input and output combinations facilitated by our specially engineered two-port dual-mode waveguide system. Such an S-matrix relation can be written as

$$\begin{bmatrix}\Psi^1\\ \Psi^2\\ \Psi^3\\ \Psi^4\end{bmatrix}_{op} = \begin{bmatrix}0 & 0 & S_{13} & S_{14}\\ 0 & 0 & S_{23} & S_{24}\\ S_{31} & S_{32} & 0 & 0\\ S_{41} & S_{42} & 0 & 0\end{bmatrix}\begin{bmatrix}\Psi^1\\ \Psi^2\\ \Psi^3\\ \Psi^4\end{bmatrix}_{in}, \tag{7}$$

which allows for a comprehensive comparison with the functionality of an analogous four-port device, as depicted in Fig. 5. In Eq. (7), a 4×4 S matrix (with the elements S_{mn}) relates the input and outputs matrices $[\Psi^n]_{in}$ and $[\Psi^m]_{op}$ with $\{m, n\} \in \{1, 2, 3, 4\}$, where $S_{mn} = \langle\Psi^n_{in}|\Psi^m_{op}\rangle$. In this context, the wave functions at the ports $\{1, 2\}$ and $\{3, 4\}$ of the four-port device mimic two supported modes $\{\Psi_F, \Psi_H\}$ at $z = 0$ and $z = l$ of our two-port waveguide system.

The 4×4 S matrix can be partitioned into four distinct 2×2 blocks. The elements of the top-left and bottom-right blocks correspond to the potential reflections at $z = 0$ and $z = l$, respectively (while considering the two-port operation), and are, thus, considered as 2×2 null matrices in order to disregard any such reflections. Consequently, the obtained S matrix captures the input-output relationships between Ψ_F and Ψ_H originating from two opposite ends. In this arrangement,

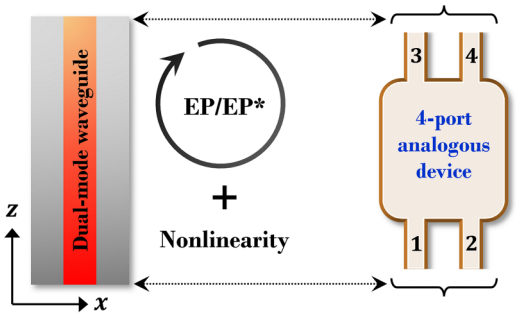

FIG. 5. A schematic analogy between a four-port optical device and our designed dual-mode waveguide operating with a dynamically encircled EP or EP* in the presence of nonlinearity. This analogy is essentially drawn to construct a 4×4 S-matrix [given by Eq. (7)] considering all the possible transmissions.

the elements in the bottom-left block correspond to the transmission from $z = 0$ to $z = l$ (forward direction), whereas the elements in the top-right block correspond to the transmission from $z = l$ to $z = 0$ (backward direction). Now, it can be understood that if $[S]$ defines the scattering matrix for WG_A, then the analytical transpose form of $[S]$ would be associated with WG_T (however, their respective matrix elements would be different, due to the presence of two opposite gain-loss profiles for WG_A and WG_T).

In the linear regime, the chirality-driven asymmetric mode conversion process in a particular waveguide variant follows Lorentz's reciprocity with a symmetric S-matrix, i.e., $[S] = [S]^T$. Now, the direction dependence on the system's response can bring up a special interest in achieving one-way transmission, which is compulsory for designing nonreciprocal devices. However, the presence of nonreciprocity obligatorily indicates the breakdown of Lorentz's reciprocity with an asymmetric S matrix, i.e., $[S] \neq [S]^T$ [46]. In this context, unidirectional transmission with a symmetric scattering matrix was reported in a photonic circuit [47], where isolation is not realizable [46,48].

To break the reciprocity in EP-induced light dynamics, we exploit the effect of local nonlinearity. We schematically represent our proposed scheme in Fig. 5 with an operational analogy between one of the designed dual-mode waveguide variants (hosting a dynamically encircled EP or EP*) with nonlinearity and a four-port isolator device. Here, we quantify a particular nonlinearity level as $N_l = (\Delta n_{NL}/\Delta n) \times 100\%$ (with $\Delta n = 0.04$; for the designed passive waveguide), where the variation of Δn_{NL} depends on the modal field-intensities ($I \equiv |\Psi|^2$) for a particular nonlinear coefficient (n_2). Here, we initially study the effect of Kerr-type nonlinearities to achieve an adequate level of nonreciprocity for both waveguide variants (in terms of an isolation ratio, say, IR) with proper optimization. Then, we also explore the effect of saturable nonlinearities to enhance the IR further and perform a quantitative comparison. We consider the forms of two different types of nonlinearities, viz.,

$$\text{Kerr-type nonlinearity:} \quad \Delta n_{NL}(x, z) = n_2 I, \tag{8a}$$

$$\text{Saturable nonlinearity:} \quad \Delta n_{NL}(x, z) = \frac{n_2 I}{1 + I/I_s}. \tag{8b}$$

I_s in Eq. (8b) defines a saturating intensity. The operations of two $\mathcal{T}$-symmetric waveguide variants in terms of nonlinearity-induced optical isolations are illustrated in Figs. 6 and 7. Figure 6 shows prototype isolation schemes for both the variants with the one-way transfer of selective modes at an optimized nonlinearity level (N_l), where Fig. 7 illustrates how we optimize such a specific N_l.

In Fig. 6(a), we show the one-way propagation of modes through WG_A (which hosts a dynamically encircled EP) with Kerr-type nonlinearity in the spatial index distribution. We judiciously optimize the nonlinearity level at $N_l = 6.75\%$. Here, we observe that the waveguide is active for the encirclement in the CW direction, where both quasiguided modes are fully transmitted from $z = 0$ to $z = l$. Moreover, the adiabatic and nonadiabatic relations [from Eq. (6)] for this specific encirclement condition allow the asymmetric conversions $\{\Psi_F, \Psi_H\} \rightarrow \Psi_H$, which results in delivery of the dominating Ψ_H at $z = l$ of WG_A. Meanwhile, for the consideration of the dynamical EP encirclement in the CCW direction, we also observe that almost no light is transmitted from $z = l$ to $z = 0$, which is shown in Fig. 6(b) via a relative intensity difference. Figure 6(b) schematically shows the prototype isolation scheme achieved using WG_A along with one of the output (O/P) field intensities at both $z = l$ and $z = 0$ (i.e., for the forward and backward transmissions, respectively, with the inputs as already shown in Fig. 1(b); as both modes are converted into a particular dominating mode for propagation in a specific direction, we obtain almost similar output intensities at a particular output-end, and hence we show only one of two output field-intensities for each of the propagation directions). Here, the dotted blue curve represents the normalized output field intensity (Ψ_H) at $z = l$, while considering the forward propagation ($z : 0 \rightarrow l$). However, during the backward propagation ($z : l \rightarrow 0$), the dotted red curve shows the output field intensity (Ψ_H) at $z = 0$, which is relative with respect to the output at $z = l$ obtained during the forward propagation (the relative output is considered to indicate the intensity difference while considering the propagation in two opposite directions). Here, output intensity at $z = 0$ decreases almost 98.6% (during the backward propagation) in comparison to the output at $z = l$ (during the forward propagation). Two outputs at $z = 0$ and $z = l$ perfectly imply the prototype isolation scheme of WG_A, which passes Ψ_H in the forward direction and blocks Ψ_F in the backward direction.

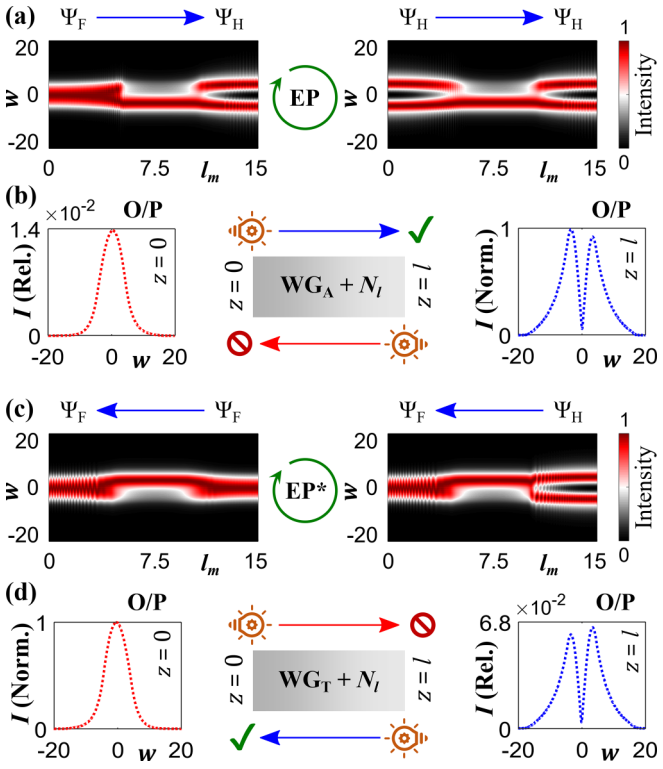

FIG. 6. (a) Nonreciprocal transition of modes with the asymmetric conversions $\{\Psi_F, \Psi_H\} \rightarrow \Psi_H$ through WG_A which is active in the forward direction ($z : 0 \rightarrow l$; associated with the CW dynamical EP encirclement process). (b) Schematic nonreciprocal response of WG_A (which allows light to pass in the forward direction, however, blocks in the backward directions) along with outputs (O/P) at $z = l$ (for the allowed path $z : 0 \rightarrow l$) and $z = 0$ (for the blocked path $z : l \rightarrow 0$. (c) Nonreciprocal transition of modes with the asymmetric conversions $\{\Psi_F, \Psi_H\} \rightarrow \Psi_F$ through WG_T which is active in the backward direction ($z : l \rightarrow 0$; associated with the CW dynamical encirclement of the EP*). (d) Schematic nonreciprocal response of WG_T (which allows light to pass in the backward direction, however, blocks in the forward directions) along with outputs (O/P) at $z = 0$ (for the allowed path $z : l \rightarrow 0$) and $z = l$ (for the blocked path $z : 0 \rightarrow l$). For both WG_A and WG_T, the self-normalized outputs are shown for their active directions, whereas relative outputs are shown in their blocked directions. w and l ($= l_m \times 10^3$) are considered in units of λ.

In Fig. 6(c), we investigate a prototype isolation scheme based on WG_T in the presence of Kerr-type nonlinearity with $N_l = 6.75\%$ (same as considered for WG_A). Here, we observe that the waveguide is surprisingly active in the backward direction ($z : l \rightarrow 0$) which is associated with the CW dynamical encirclement scheme around the EP*. The waveguide passes the dominating Ψ_F [based on the corresponding nonadiabatic correction factors from Eq. (6)] with the asymmetric conversions $\{\Psi_F, \Psi_H\} \rightarrow \Psi_F$, as can be observed via the associated beam propagation results. The light becomes blocked in the forward direction, which is associated with the CCW dynamical encirclement process around the EP*. The prototype isolation scheme along with the output (O/P) field intensities for WG_T are shown in Fig. 6(d). From the normalized output intensity at $z = 0$ (Ψ_F; during the backward propagation) and relative output intensity at $z = l$ (Ψ_H; during the forward propagation; relative with respect to the output Ψ_F at $z = 0$), it is clearly evident that the intensity decreases ≈93.3% during the forward propagation through WG_T. Hence, WG_T allows Ψ_F to pass in the backward direction, however, blocks Ψ_H in the forward direction.

Hence, at a particular nonlinearity level, both $\mathcal{T}$-symmetric waveguide variants behave as isolators, which allow the nonreciprocal transmission of two different selective modes in opposite directions. For a particular variant, a breakdown of the inversion symmetry in the length-depended gain-loss variation occurs in two opposite directions, where the tailored nonlinearity induces nonreciprocity. Hence, the intensity of the incoming waves becomes completely attenuated in a particular direction, despite being transmitted fully in the opposite direction. Here, a correlation between the

nonreciprocal transmissions to two different allowed modes in two waveguide variants is dictated by the nonadiabatic corrections around EP and EP*. It is crucial to emphasize that the influence of dynamic nonreciprocity, primarily arising from the reciprocity relations associated with small-amplitude additional waves in the presence of Kerr or Kerr-like nonlinearities [49], can effectively be disregarded in our proposed approach. This is attributable to the chosen configuration and operating conditions specifically tailored for a single frequency. Here, both variants of the waveguide block any backward noise at the selected operating frequency.

Now, we quantify maximum nonreciprocity in terms of an IR for both the waveguide variants. For a particular two-port waveguide device, the IR can be defined as a quantitative measurement (in dB) of the difference between the transmissions in the active and inactive directions

$$\mathrm{IR\,(dB)} = 10\log_{10}\left[\frac{T_{\mathrm{active}}}{T_{\mathrm{inactive}}}\right] = 10\log_{10}\left|\frac{S_{mn}}{S_{nm}}\right|^2. \quad (9)$$

Taking into account two transitions permitted by the adiabatic and nonadiabatic relations around the EP/EP* [as shown in Fig. 6; governed by Eq. (6)], we present the higher value of IR (maximum nonreciprocity) achieved for a particular waveguide variant and consider the respective S_{mn} from the associated S matrix. The higher value of IR is consistently observed during adiabatic transitions for both waveguide variants. However, for a specific variant, it is noteworthy that the IR values associated with both the allowed transitions are closely situated. We determine the maximum nonreciprocity for $\mathrm{WG_A}$ as 18.6 dB using $\mathrm{IR} = 10\log_{10}|S_{41}/S_{14}|^2$. Whereas, the maximum nonreciprocity for $\mathrm{WG_T}$ is estimated at 11.75 dB via $\mathrm{IR} = 10\log_{10}|S_{14}/S_{41}|^2$.

Such an exclusive nonreciprocal transmission of selective modes mainly relies on the interplay between dynamical gain-loss variation (active components) and the tailored local nonlinearity in the spatial index distribution (passive components). During the propagation of light around an EP in the presence of nonlinearity, the complex β values of the supported modes become affected significantly. The EP-induced interactions are led by the variations of both $\mathrm{Re}(\beta)$ (modal confinement) and $\mathrm{Im}(\beta)$ (decay rates), where the incorporation of nonlinearity directly influences $\mathrm{Re}(\beta)$. Now, the mode confinement factors enhance with an increasing amount of nonlinearity, which results in the simultaneous reduction of the associated decay rates. Hence, the onset of nonlinearity modifies the gain-loss parameter space concerning the location of the EP (or EP*), and accordingly the relative-gain factor [$\Delta\gamma^{\mathrm{ad}}_{\mathrm{F,H}}$; associated with Eq. (6)] between the interacting modes is affected significantly during the evolution of modes following the dynamical EP-encirclement scheme. Based on such an interplay, the relative intensity difference at two opposite output-ends varies for different nonlinearity amounts, which can be understood from the variation of the IR concerning the nonlinearity level (N_l), as shown in Fig. 7(a).

The IR initially increases with an increasing Kerr-type nonlinearity level and takes a maximum value of 18.6 dB for $\mathrm{WG_A}$ and 11.75 dB for $\mathrm{WG_T}$ at a certain threshold nonlinearity-level of $N_l = 6.75\%$ [as shown in Fig. 7(a)]. Here, the difference in the IR for two waveguide variants at a particular N_l can be observed, which occurs due to a different gain-loss profile (exactly opposite; based on $\mathcal{T}$ symmetry) as can be seen in Fig. 3(b). The operation of $\mathrm{WG_A}$ is mainly dominated by loss, whereas $\mathrm{WG_T}$ operates with an overall higher amount of gain. Hence, $\mathrm{WG_A}$ is able to induce a comparably higher output intensity difference for the light propagation in two opposite directions. An additional gain-amplification in $\mathrm{WG_T}$ might reduce such intensity difference between two outputs, which results in achieving a lower IR for $\mathrm{WG_T}$ in comparison to $\mathrm{WG_A}$ at a particular N_l. However, we interestingly observe that both waveguide variants achieve their highest IR at a specific $N_l = 6.75\%$, which affirms their operational correlation based on the chiral behavior of two conjugate EPs. It is further noticeable that while increasing N_l more than 6.75%, the IR decreases gradually [as shown in Fig. 7(a)] for both variants. Such a decrease of the IR after a certain threshold is mainly due to the abrupt effect of nonlinearity on the encirclement loop that affects the location of the EP significantly (i.e., the EP might come closer to the boundary of the modified loop in the parameter space due to a higher amount of nonlinearity). Here, judicious care should be taken to optimize the N_l, as a higher nonlinearity after a certain limit may exclude the EP from the parametric loop, for which the overall observation might be intangible. However, there is a sufficient scope of scalability to investigate the device operation for different amounts of nonlinearities within a broad range. The characteristic curve shown in Fig. 7(a) essentially defines the process to choose an optimized nonlinearity amount, from where we set $N_l = 6.75\%$ to obtain the beam propagation results in Fig. 6.

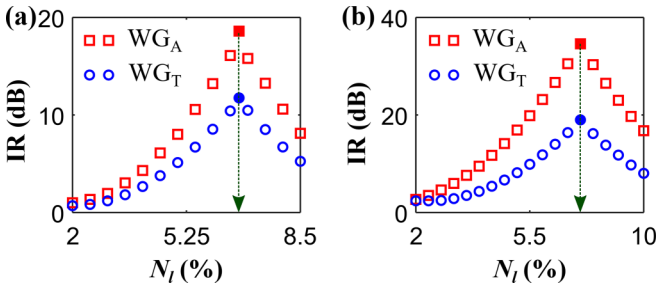

FIG. 7. Dependence of the isolation ratio (IR) on the local nonlinearity level (N_l), while considering (a) Kerr-type nonlinearity and (b) saturable nonlinearity, separately. Red square and blue circular markers show such a variation of IR for $\mathrm{WG_A}$ and $\mathrm{WG_T}$, respectively. The green arrows in both (a) and (b) indicate the largest values of the IRs, as achieved at the same N_l.

Then, instead of local Kerr-type nonlinearity, we introduce saturable nonlinearity in the spatial index distribution to investigate the nonreciprocal transmission through $\mathrm{WG_A}$ and $\mathrm{WG_T}$. The saturable nonlinearity is considered with a chosen saturating intensity [I_s; as per Eq. (8b)] based on the materials of the background waveguide. For Kerr-type nonlinearity, a nonlinear interaction of light in the optical medium gradually increases with an increasing signal intensity, which might ensemble instability in the output signals after a certain limit. In this context, the consideration of the saturable intensity in the associated nonlinear interactions can potentially stabilize the output signals, where we can observe a higher intensity

difference at two output ends for propagation in the opposite directions. Hence, we optimize the saturable nonlinearity level at 7.5% from the characteristic dependence of the IR on N_l, as shown in Fig. 7(b). Here, we observe an exactly similar nonreciprocal response of both WG_A and WG_T, as we have seen for the choice of Kerr-type nonlinearity in Fig. 6. WG_A allows the nonreciprocal transmission of Ψ_H in the forward direction, whereas isolates Ψ_F in the backward direction. The field intensity decreases ≈99.96% during the backward propagation, where we achieve a maximum of the IR of 34.6 dB. On the other hand, we achieve a maximum of 18.6 dB IR for WG_T, which allows Ψ_F to transmit along the backward direction and isolates Ψ_H in the forward direction with almost 98.7% reduction of the signal intensity.

III. SUMMARY

In summary, a significant stride in understanding and utilizing the concept of conjugate EPs has been made in the context of a correlative nonreciprocal light transmission process. Based on the hosting of two dynamically encircled conjugate EPs in two $\mathcal{T}$-symmetric variants of a planar gain-loss assisted waveguide, a comprehensive all-optical scheme has been established with the introduction of local nonlinearity, where we revealed a specific chiral correlation between the nonreciprocal responses of two underlying waveguide variants. Here, two $\mathcal{T}$-symmetric waveguide variants, hosting two conjugate EPs, are characterized by their ability to behave as isolators enabling nonreciprocal transmission of selective modes in opposite directions. They allow active transmission of two different dominant modes in opposite directions, whereas block light from passing in their respective reverse directions. We investigated the effect of both Kerr-type and saturable nonlinearities on achieving nonreciprocity, where we observed that the onset of saturable nonlinearity can induce a comparably higher nonreciprocal effect. The intricate interplay of the dynamical gain-loss parameter space around the conjugate EPs in the presence of different types of nonlinearities were discussed in detail to understand such unconventional chiral nonreciprocal light dynamics. The isolation ratio for both waveguide variants has been precisely evaluated across varying nonlinearity levels, where we achieved a huge isolation ratio, even up to 34.6 dB, under a specific operating condition. This notable outcome underscores the efficacy of our approach. Moreover, there exists a considerable potential to enhance the device's performance further by strategically scaling geometrical parameters, optimizing gain-loss configurations, and adjusting nonlinearity. Based on the proposed scheme, a nonreciprocal mode-selective four-port circulatory operation can be explored by using an appropriate coupled optical system designed with two underlying $\mathcal{T}$-symmetric nonlinear waveguides. The insights and implementations of our approach harnessing the fascinating features of conjugate EPs in nonlinear optical systems would unlock a new avenue with exciting possibilities for boosting the development of various nonreciprocal components, such as optical isolators and circulators, for integrated (on-chip) photonic applications in next-generation communication networks and quantum information processing.

ACKNOWLEDGMENTS

A.L. and A.M. acknowledge the financial support from the Maestro Grant of the Polish National Science Center (NCN) (Grant No. DEC-2019/34/A/ST2/00081). A.L. also acknowledges the support from the National Postdoctoral Fellowship Scheme of the Science and Engineering Research Board (SERB) under the Govt. of India (Grant No. PDF/2021/001322).

APPENDIX: AN ANALYTICAL APPROACH TOWARD HOSTING CONJUGATE EXCEPTIONAL POINTS

The occurrence of conjugate EPs in any physical system can be understood as a mathematical problem by constructing an analogous 2×2 non-Hermitian Hamiltonian given by

$$\mathcal{H}(\lambda) = \mathcal{H}_0 + \lambda\mathcal{H}_p = \begin{pmatrix} \beta_1 & 0 \\ 0 & \beta_2 \end{pmatrix} + \lambda \begin{pmatrix} \kappa_1 & \gamma_1 \\ \gamma_2 & \kappa_2 \end{pmatrix}. \quad \text{(A1)}$$

Here, a passive Hamiltonian $\mathcal{H}_0$, consisting of two passive eigenvalues β_j $(j = 1, 2)$, is subjected by a perturbation $\mathcal{H}_p$, which is dependent on some coupling parameters κ_j and γ_j $(j = 1, 2)$ with a perturbation strength λ.

A trivial case can be considered with real-valued β_j, κ_j, and λ along with $\gamma_j = 0$, for which the effective Hamiltonian $\mathcal{H}$ behaves as a Hermitian system and possesses two distinct eigenvalues: $\mathcal{E}_j(\lambda) = \beta_j + \lambda\,\kappa_j$ $(j = 1, 2)$. Here, a conventional degeneracy occurs at $\lambda = -(\beta_1 - \beta_2)/(\kappa_1 - \kappa_2)$. Now, to ensure the system to be non-Hermitian, all the elements in $\mathcal{H}_p$ might be chosen as nonzero with a complex λ, where $[H_0, H_p] \neq 0$. The operation of our designed dual mode waveguide based optical system can be understood based on such a non-Hermitian Hamiltonian. Here, β_1 and β_2 represent two real propagation constants. The complex λ defines the overall non-Hermitian elements based on gain-loss parameters κ_j and γ_j $(j = 1, 2)$, where κ_j can be appeared as individual modal decay rates, whereas γ_j can be considered as introduced gain-loss elements.

The eigenvalues of $\mathcal{H}$ can generically be written as

$$\mathcal{E}_{1,2}(\lambda) = \frac{\beta_1 + \beta_2 + \lambda(\kappa_1 + \kappa_2)}{2} \pm R, \quad \text{(A2)}$$

where

$$R = \left[\left(\frac{\beta_1 - \beta_2}{2} \right)^2 + \lambda^2 \left\{ \left(\frac{\kappa_1 - \kappa_2}{2} \right)^2 + \gamma_1\gamma_2 \right\} + \frac{\lambda}{2}(\beta_1 - \beta_2)(\kappa_1 - \kappa_2) \right]^{1/2}. \quad \text{(A3)}$$

Owing to the coupling invoked by finite γ_j $(j = 1, 2)$, two levels $\mathcal{E}_1$ and $\mathcal{E}_2$ exhibit avoided resonance crossing (ARC; i.e., two levels do not cross but avoid each other) type interactions with a continuous variation of λ. While exhibiting ARCs, the two levels coalesce at two critical values of λ, which represent a complex conjugate pair of EPs in the complex λ-plane. These two singularities can be obtained in the complex λ-plane by setting $R = 0$, which are given by

$$\lambda_s^{\pm} = -\frac{(\beta_1 - \beta_2)}{(\kappa_1 - \kappa_2) \mp 2i\sqrt{\gamma_1\gamma_2}}. \quad \text{(A4)}$$

The connection between two conjugate EPs can be understood by rewriting R in terms of λ_s^+ and λ_s^- as

$$R = \sqrt{\left(\frac{\lambda-\lambda_s^+}{2}\right)\left\{\left(\frac{\kappa_1-\kappa_2}{2}\right)^2+\gamma_1\gamma_2\right\}\left(\frac{\lambda-\lambda_s^-}{2}\right)}. \tag{A5}$$

Hence, the coupled levels are specified by the value of $\sqrt{\lambda-\lambda_s^+}$ and $\sqrt{\lambda-\lambda_s^-}$ on two different Riemann surfaces. The critical eigenvalues at two conjugate EPs (i.e., at λ_s^+ and λ_s^-) are given by

$$\mathcal{E}_s(\lambda_s^\pm) = \frac{(\kappa_1\beta_2-\kappa_2\beta_1)\mp i\sqrt{\gamma_1\gamma_2}(\beta_1+\beta_2)}{(\kappa_1-\kappa_2)\mp 2i\sqrt{\gamma_1\gamma_2}}. \tag{A6}$$

Now, an EP is associated with the occurrence of only one independent eigenvector, unlike two orthogonal eigenvectors at a trivial Hermitian degeneracy. Thus, using the biorthogonal norm for a non-Hermitian Hamiltonian, two right-hand eigenvectors at two conjugate EPs (one for each of the EPs) can be written as (approximated up to a factor)

$$|\Psi_s^+\rangle = \begin{pmatrix} +i\gamma_1 \\ \sqrt{\gamma_1\gamma_2} \\ 1 \end{pmatrix} \quad \text{for} \quad \lambda=\lambda_s^+, \tag{A7a}$$

$$|\Psi_s^-\rangle = \begin{pmatrix} -i\gamma_1 \\ \sqrt{\gamma_1\gamma_2} \\ 1 \end{pmatrix} \quad \text{for} \quad \lambda_s=\lambda_s^-, \tag{A7b}$$

with the associated left-hand eigenvectors

$$\langle\widetilde{\Psi}_s^+| = \begin{pmatrix} +i\gamma_2 \\ \sqrt{\gamma_1\gamma_2} \end{pmatrix} \quad 1 \qquad \text{for} \quad \lambda=\lambda_s^+, \tag{A8a}$$

$$\langle\widetilde{\Psi}_s^-| = \begin{pmatrix} -i\gamma_2 \\ \sqrt{\gamma_1\gamma_2} \end{pmatrix} \quad 1 \qquad \text{for} \quad \lambda=\lambda_s^-. \tag{A8b}$$

From Eqs. (A1) and (A2), it is evident that

$$\langle\widetilde{\Psi}_s^+|\Psi_s^+\rangle = 0 \qquad \text{and} \qquad \langle\widetilde{\Psi}_s^-|\Psi_s^-\rangle = 0. \tag{A9}$$

These conditions are referred to as the self-orthogonality that holds at both the conjugate EPs. The existence of only one self-orthogonal eigenvector reflects the fact that the Hamiltonian $\mathcal{H}(\lambda)$ becomes nondiagonalizable for both $\lambda=\lambda_s^+$ or λ_s^-, i.e., at the two conjugate EPs.

[1] B. Midya, H. Zhao, and L. Feng, Non-Hermitian photonics promises exceptional topology of light, Nat. Commun. **9**, 2674 (2018).

[2] T. Kato, *Perturbation Theory for Linear Operators* (Springer, Berlin, 1966).

[3] W. D. Heiss, Repulsion of resonance states and exceptional points, Phys. Rev. E **61**, 929 (2000).

[4] M. V. Berry, Physics of nonhermitian degeneracies, Czech. J. Phys. **54**, 1039 (2004).

[5] W. D. Heiss, The physics of exceptional points, J. Phys. A: Math. Theor. **45**, 444016 (2012).

[6] H. Eleuch and I. Rotter, Clustering of exceptional points and dynamical phase transitions, Phys. Rev. A **93**, 042116 (2016).

[7] C. M. Bender and S. Boettcher, Real spectra in non-Hermitian Hamiltonians having *PT* symmetry, Phys. Rev. Lett. **80**, 5243 (1998).

[8] C. M. Bender, Making sense of non-Hermitian Hamiltonians, Rep. Prog. Phys. **70**, 947 (2007).

[9] A. Guo, G. J. Salamo, D. Duchesne, R. Morandotti, M. Volatier-Ravat, V. Aimez, G. A. Siviloglou, and D. N. Christodoulides, Observation of $\mathcal{PT}$-symmetry breaking in complex optical potentials, Phys. Rev. Lett. **103**, 093902 (2009).

[10] C. E. Rüter, K. G. Makris, R. El-Ganainy, D. N. Christodoulides, M. Segev, and D. Kip, Observation of parity–time symmetry in optics, Nat. Phys. **6**, 192 (2010).

[11] R. El-Ganainy, K. G. Makris, M. Khajavikhan, Z. H. Musslimani, S. Rotter, and D. N. Christodoulides, Non-Hermitian physics and PT symmetry, Nat. Phys. **14**, 11 (2018).

[12] Ş. K. Özdemir, S. Rotter, F. Nori, and L. Yang, Parity–time symmetry and exceptional points in photonics, Nat. Mater. **18**, 783 (2019).

[13] M.-A. Miri and A. Alù, Exceptional points in optics and photonics, Science **363**, eaar7709 (2019).

[14] E. J. Bergholtz, J. C. Budich, and F. K. Kunst, Exceptional topology of non-Hermitian systems, Rev. Mod. Phys. **93**, 015005 (2021).

[15] C. Wang, Z. Fu, W. Mao, J. Qie, A. D. Stone, and L. Yang, Non-Hermitian optics and photonics: from classical to quantum, Adv. Opt. Photon. **15**, 442 (2023).

[16] Q. Yan, B. Zhao, R. Zhou, R. Ma, Q. Lyu, S. Chu, X. Hu, and Q. Gong, Advances and applications on non-Hermitian topological photonics, Nanophotonics **12**, 2247 (2023).

[17] M. Parto, Y. G. N. Liu, B. Bahari, M. Khajavikhan, and D. N. Christodoulides, Non-Hermitian and topological photonics: optics at an exceptional point, Nanophotonics **10**, 403 (2021).

[18] H. Xu, D. Mason, L. Jiang, and J. G. E. Harris, Topological energy transfer in an optomechanical system with exceptional points, Nature (London) **537**, 80 (2016).

[19] I. I. Arkhipov, A. Miranowicz, F. Minganti, Ş. K. Özdemir, and F. Nori, Dynamically crossing diabolic points while encircling exceptional curves: A programmable symmetric-asymmetric multimode switch, Nat. Commun. **14**, 2076 (2023).

[20] A. Laha, D. Beniwal, and S. Ghosh, Successive switching among four states in a gain-loss-assisted optical microcavity hosting exceptional points up to order four, Phys. Rev. A **103**, 023526 (2021).

[21] J. Zhang, B. Peng, Ş. K. Özdemir, K. Pichler, D. O. Krimer, G. Zhao, F. Nori, Y.-x. Liu, S. Rotter, and L. Yang, A phonon laser operating at an exceptional point, Nat. Photonics **12**, 479 (2018).

[22] C. Wang, W. R. Sweeney, A. D. Stone, and L. Yang, Coherent perfect absorption at an exceptional point, Science **373**, 1261 (2021).

[23] T. Goldzak, A. A. Mailybaev, and N. Moiseyev, Light stops at exceptional points, Phys. Rev. Lett. **120**, 013901 (2018).
[24] L. J. Fernández-Alcázar, R. Kononchuk, and T. Kottos, Enhanced energy harvesting near exceptional points in systems with (pseudo-)PT-symmetry, Commun. Phys. **4**, 79 (2021).
[25] A. A. Zyablovsky, E. S. Andrianov, and A. A. Pukhov, Parametric instability of optical non-Hermitian systems near the exceptional point, Sci. Rep. **6**, 29709 (2016).
[26] W. Chen, Ş. K. Özdemir, G. Zhao, J. Wiersig, and L. Yang, Exceptional points enhance sensing in an optical microcavity, Nature (London) **548**, 192 (2017).
[27] J. Wiersig, Review of exceptional point-based sensors, Photon. Res. **8**, 1457 (2020).
[28] A. Laha, S. Dey, and S. Ghosh, Reverse-chiral response of two $\mathcal{T}$-symmetric optical systems hosting conjugate exceptional points, Phys. Rev. A **105**, 022203 (2022).
[29] I. Gilary, A. A. Mailybaev, and N. Moiseyev, Time-asymmetric quantum-state-exchange mechanism, Phys. Rev. A **88**, 010102(R) (2013).
[30] T. J. Milburn, J. Doppler, C. A. Holmes, S. Portolan, S. Rotter, and P. Rabl, General description of quasiadiabatic dynamical phenomena near exceptional points, Phys. Rev. A **92**, 052124 (2015).
[31] C. Dembowski, B. Dietz, H.-D. Gräf, H. L. Harney, A. Heine, W. D. Heiss, and A. Richter, Encircling an exceptional point, Phys. Rev. E **69**, 056216 (2004).
[32] J. Doppler, A. A. Mailybaev, J. Böhm, U. Kuhl, A. Girschik, F. Libisch, T. J. Milburn, P. Rabl, N. Moiseyev, and S. Rotter, Dynamically encircling an exceptional point for asymmetric mode switching, Nature (London) **537**, 76 (2016).
[33] X.-L. Zhang and C. T. Chan, Dynamically encircling exceptional points in a three-mode waveguide system, Commun. Phys. **2**, 63 (2019).
[34] A. Laha, A. Biswas, and S. Ghosh, Nonadiabatic modal dynamics around exceptional points in an all-lossy dual-mode optical waveguide: Toward chirality-driven asymmetric mode conversion, Phys. Rev. Appl. **10**, 054008 (2018).
[35] S. Dey, A. Laha, and S. Ghosh, Nonlinearity-induced anomalous mode collapse and nonchiral asymmetric mode switching around multiple exceptional points, Phys. Rev. B **101**, 125432 (2020).
[36] A. Laha, S. Dey, H. K. Gandhi, A. Biswas, and S. Ghosh, Exceptional point and toward mode-selective optical isolation, ACS Photonics **7**, 967 (2020).
[37] R. Thomas, H. Li, F. M. Ellis, and T. Kottos, Giant nonreciprocity near exceptional-point degeneracies, Phys. Rev. A **94**, 043829 (2016).
[38] Y. Choi, C. Hahn, J. W. Yoon, S. H. Song, and P. Berini, Extremely broadband, on-chip optical nonreciprocity enabled by mimicking nonlinear anti-adiabatic quantum jumps near exceptional points, Nat. Commun. **8**, 14154 (2017).
[39] C. Caloz, A. Alù, S. Tretyakov, D. Sounas, K. Achouri, and Z.-L. Deck-Léger, Electromagnetic nonreciprocity, Phys. Rev. Appl. **10**, 047001 (2018).
[40] F. Minganti, A. Miranowicz, R. W. Chhajlany, and F. Nori, Quantum exceptional points of non-Hermitian Hamiltonians and liouvillians: The effects of quantum jumps, Phys. Rev. A **100**, 062131 (2019).
[41] F. Minganti, A. Miranowicz, R. W. Chhajlany, I. I. Arkhipov, and F. Nori, Hybrid-Liouvillian formalism connecting exceptional points of non-Hermitian Hamiltonians and Liouvillians via postselection of quantum trajectories, Phys. Rev. A **101**, 062112 (2020).
[42] A. A. Zyablovsky, A. P. Vinogradov, A. V. Dorofeenko, A. A. Pukhov, and A. A. Lisyansky, Causality and phase transitions in $\mathcal{PT}$-symmetric optical systems, Phys. Rev. A **89**, 033808 (2014).
[43] S. Phang, A. Vukovic, S. C. Creagh, T. M. Benson, P. D. Sewell, and G. Gradoni, Parity-time symmetric coupled microresonators with a dispersive gain/loss, Opt. Express **23**, 11493 (2015).
[44] G. P. Agrawal, *Nonlinear Fiber Optics*, 4th ed. (Academic, New York, 2007).
[45] A. Roy, S. Dey, A. Laha, A. Biswas, and S. Ghosh, Exceptional-point-induced asymmetric mode conversion in a dual-core optical fiber segment, Opt. Lett. **47**, 2546 (2022).
[46] D. Jalas, A. Petrov, M. Eich, W. Freude, S. Fan, Z. Yu, R. Baets, M. Popović, A. Melloni, J. D. Joannopoulos, M. Vanwolleghem, C. R. Doerr, and H. Renner, What is—and what is not—an optical isolator, Nat. Photonics **7**, 579 (2013).
[47] L. Feng, M. Ayache, J. Huang, Y.-L. Xu, M.-H. Lu, Y.-F. Chen, Y. Fainman, and A. Scherer, Nonreciprocal light propagation in a silicon photonic circuit, Science **333**, 729 (2011).
[48] S. Fan, R. Baets, A. Petrov, Z. Yu, J. D. Joannopoulos, W. Freude, A. Melloni, M. Popovi, M. Vanwolleghem, D. Jalas, M. Eich, M. Krause, H. Renner, E. Brinkmeyer, and C. R. Doerr, Comment on "Nonreciprocal light propagation in a silicon photonic circuit", Science **335**, 38 (2012).
[49] Y. Shi, Z. Yu, and S. Fan, Limitations of nonlinear optical isolators due to dynamic reciprocity, Nat. Photonics **9**, 388 (2015).